JOURNAL OF GEOPHYSICAL RESEARCH, VOL. 112, D04108, doi:10.1029/2006JD007410, 2007



# Observations and simulations of synoptic, regional, and local variations in atmospheric $CO_2$

Jih-Wang Wang,[1,2] A. Scott Denning,[1] Lixin Lu,[1] Ian T. Baker,[1] Katherine D. Corbin,[1] and Kenneth J. Davis[3]

Received 15 April 2006; revised 17 July 2006; accepted 20 September 2006; published 28 February 2007.

[1] Synoptic events may play an important role in determining the $CO_2$ spatial distribution and temporal variations on a regional scale. In this study, we chose a front that passed the WLEF tower site on 16 August 2001, which had the most significant $CO_2$ concentration variation in our case pool. The $CO_2$ concentration, or [$CO_2$], at the WLEF site had a strong dip and an increasing trend before the front arrived and a decreasing trend afterward. The concentration at 396 m above the ground varied by more than 40 ppm within 36 hours. We investigated the $CO_2$ variations associated with this frontal case using a fully coupled model of land surface physics and carbon exchange (SiB 2.5) and the atmosphere (RAMS 5.04), in which $CO_2$ was treated as a free variable and used to determine photosynthesis rate. Our simulation showed that high-[$CO_2$] air mass was built up in the southern Great Plains on 14 and15 August 2001 because of the slow photosynthesis rate caused by hot and dry air over Oklahoma and Texas and the relatively strong nighttime respiration in the southeast United States. The low-[$CO_2$] air to the southwest of Wisconsin and the high-[$CO_2$] air over Kansas and Oklahoma traveled north and was responsible for part of the [$CO_2$] variations at the WLEF site from 15 to 16 August 2001. Surface weather station confirmed the hot and dry weather in Oklahoma and Texas in this event, and the tower observations corroborated the existence of southwest-northeast concentration gradient. Weak daytime photosynthesis on 15 August 2001 and stronger nighttime respiration on 16 August 2001 under overcast sky condition were also partially responsible for the quick $CO_2$ accumulation at the lower levels at the WLEF site before the front's arrival. This case study confirmed the existence of mixing signals from at least two different scales: large-scale horizontal advection and local ecosystem response to the changing weather. SiB-RAMS showed its strength in simulating the coherent anomalies in biospheric $CO_2$ flux and in the regional weather pattern. Further refinement of the model is needed to better capture the timing and location of synoptic events and $CO_2$ signals that travel across North America. Exploitation of continuous tower data in data assimilation and inverse modeling to determine regional sources and sinks will require careful error attribution to either transport or surface flux estimates.

**Citation:** Wang, J.-W., A. S. Denning, L. Lu, I. T. Baker, K. D. Corbin, and K. J. Davis (2007), Observations and simulations of synoptic, regional, and local variations in atmospheric $CO_2$, *J. Geophys. Res.*, *112*, D04108, doi:10.1029/2006JD007410.

## 1. Introduction

[2] Fossil fuel burning, deforestation, cement manufacture, and land use change have resulted in more than 30% increase in the atmospheric concentration of carbon dioxide ($CO_2$) since the late 19th century. $CO_2$ concentration, or [$CO_2$], in the atmosphere has risen from 280 ppmv (parts per million by volume of dry air) before the industrial revolution, to more than 375 ppmv at present (NOAA/ESRL GMD, formerly CMDL, see http://www.cmdl.noaa.gov). However, the rate of [$CO_2$] increase in the atmosphere is estimated to be only about half the amount that is being emitted each year by fossil fuel burning [*Andres et al.*, 1996], which is currently the primary anthropogenic source of $CO_2$ into the air. It is important to understand the sink mechanisms and their variations in space and time to better understand and manage Earth system responses to the atmospheric $CO_2$ burden.

[1]Department of Atmospheric Science, Colorado State University, Fort Collins, Colorado, USA.
[2]Now at Cooperative Institute for Research in the Environmental Sciences and Department of Atmospheric and Oceanic Sciences, University of Colorado at Boulder, Boulder, Colorado, USA.
[3]Department of Meteorology, Pennsylvania State University, University Park, Pennsylvania, USA.


0148-0227/07/2006JD007410$09.00

[3] The carbon observation system is expected to undergo dramatic enhancement in the second half of this decade as additional stations are deployed as part of global observation programs [*Bender et al.*, 2002], such as the North American Carbon Program [*Wofsy and Harris*, 2002] and a similar effort in Europe (CarboEurope Integrated Project—Assessment of the European Terrestrial Carbon Balance, available at http://www.carboeurope.org). The increased density of in situ observations should enable researchers to estimate sources/sinks to a higher degree of confidence over much finer spatial scales than has been possible to date. For instance, *Hurwitz et al.* [2004] showed that their single-point high-frequency [$CO_2$] data exhibited large variations associated with synoptic weather events that could be traced to estimate upstream fluxes due to passing weather disturbances. *Law et al.* [2002] showed significant improvement in subcontinental flux retrieved in a global transport inversion of high-frequency pseudo data relative to monthly mean observations.

[4] As enhanced observations enable fluxes to be estimated at a finer resolution, errors in simulated atmospheric transport are likely to become more problematic. Improved atmospheric models may be required, which can generate fine-resolution transport information to resolve signals in the high-frequency measurements. Successful regional forward modeling is necessary to gain confidence in our ability to perform regional inverse modeling and quantify regional-scale $CO_2$ sources and sinks.

[5] Many efforts have been made to reproduce both regional and local $CO_2$ variation signals. *Geels et al.* [2004] adopted a high-resolution terrestrial biospheric model (the NCAR Land Surface Model, LSM) and a three-dimensional atmospheric transport model (the Danish Eulerian Hemispherical Model, DEHM) to reproduce $CO_2$ spatial and temporal variations. Their model still had the rigid constraint, as do in many others, in which the meteorological data were prescribed, not a variable. Therefore, although their model simulated the $CO_2$ variation very well, the model did not possess predictive skill for either the meteorology or the interaction between the land and the atmosphere. *Lu et al.* [2005] prescribed diurnal cycle of surface $CO_2$ fluxes for two different dominant biome types and showed that the mesoscale circulation was caused by the interaction of prevalent wind and topography in the Tapajos Region, Brazil, and largely determined the [$CO_2$] temporal variation at the nearby tower sites. *Denning et al.* [2003] coupled a regional atmospheric model (RAMS) with a land surface model (SiB2) that could compute biospheric $CO_2$ flux at each model time step. They used the coupled system to investigate vertical and diurnal $CO_2$ variations in the planetary boundary layer. *Nicholls et al.* [2004] used the same coupled SiB-RAMS model to study mesoscale variations over a 5-day period, and highlighted the importance of advection in the presence of large lakes. *Chan et al.* [2004] investigated the $CO_2$ exchange between the biosphere and the atmosphere by coupling the Mesoscale Compressible Community Model (MC2 [*Benoit et al.*, 1997]) with the Boreal Ecosystem Productivity Simulator (BEPS [*Liu et al.*, 2002]). They showed that synoptic and mesoscale processes had strong impacts on [$CO_2$] field evolution. They attributed changes to cloud radiative forcing on the regional ecosystem response.

[6] We used a fully coupled biosphere-atmosphere model to simulate $CO_2$ sources and sinks in order to study $CO_2$ temporal and spatial variations. The objectives of this study were (1) to interpret the variations of $CO_2$ in a frontal event with regard to the ecosystem response to weather changes, vertical mixing, and horizontal advection; (2) to investigate the $CO_2$ dip and rise before a cold front arrived at the WLEF tower in central Wisconsin for 15–16 August 2001 and the postfrontal decreasing trend; and (3) to further integrate the atmospheric model and land surface model, which will facilitate future work in understanding regional $CO_2$ sources and sinks.

[7] In section 2, a frontal case in mid-August 2001 will be described, with a very large [$CO_2$] variation that was detected in northern Wisconsin. In section 3, data preparation, model descriptions, coupling issues, and model configurations will be discussed. In section 4, the simulation results will be shown and tower data will be compared with them qualitatively. In the final section we will offer conclusions.

## 2. Case Description: Tower Observations, Site Description, and Synoptic Situation of August 2001

[8] The 447-m WLEF TV tower is located in the Chequamegon National Forest, 14 km east of Park Falls, Wisconsin. Measurements of meteorological variables and [$CO_2$] are made at 11, 30, 76, 122, 244, and 396 m on the tower, and fluxes of latent and sensible heat and [$CO_2$] are made by eddy covariance at 30, 122, and 396 m [*Davis et al.*, 2003]. The $CO_2$ data are available every 12 min, and the measurement frequency for temperature, water vapor mixing ratio, wind speed, and wind direction is 5 Hz. This site was chosen because measurements made from the mid–boundary layer reflect the influence from a large heterogeneous area of the order of $10^6$ $km^2$ [*Gloor et al.*, 2001]. The 396-m level of the WLEF tower is one of the highest equipped levels for continuous $CO_2$ variations in North America, reaching well into the mixed layer and remaining above the nocturnal inversion on nearly all nights. The typical range of the [$CO_2$] diurnal cycle in summer at the 396 m level is about 10 ppm.

[9] For the months of June, July, and August of 1997 through 2001, 51 cold fronts passing through the WLEF tower site were identified from surface weather maps. We further confirmed the fronts using the tower data when the wind direction shifted from southwest to northwest for all the three equipped levels (30 m, 122 m, and 396 m), in which wind direction was measured. Because of data fragmentation and ambiguous wind direction changes, only 12 out of 51 cases were considered. We chose to simulate the case with the largest [$CO_2$] variation (>40 ppm within 36 hours) during the frontal passage out of the 12 cases.

[10] A low-pressure system formed in the southwestern part of Ontario, Canada on 15 August and moved southeast to Lake Superior on 16 August. The wind blew from the northwest at the WLEF tower when the cold front was established from the center of the low, which stretched southwest and extended to Nebraska. At 1000 UT, 16 August, the WLEF observations at 396 m show a wind direction change from southwest to northwest. A cold front passed the tower at 1300 UT 16 August 2001, and at 0200

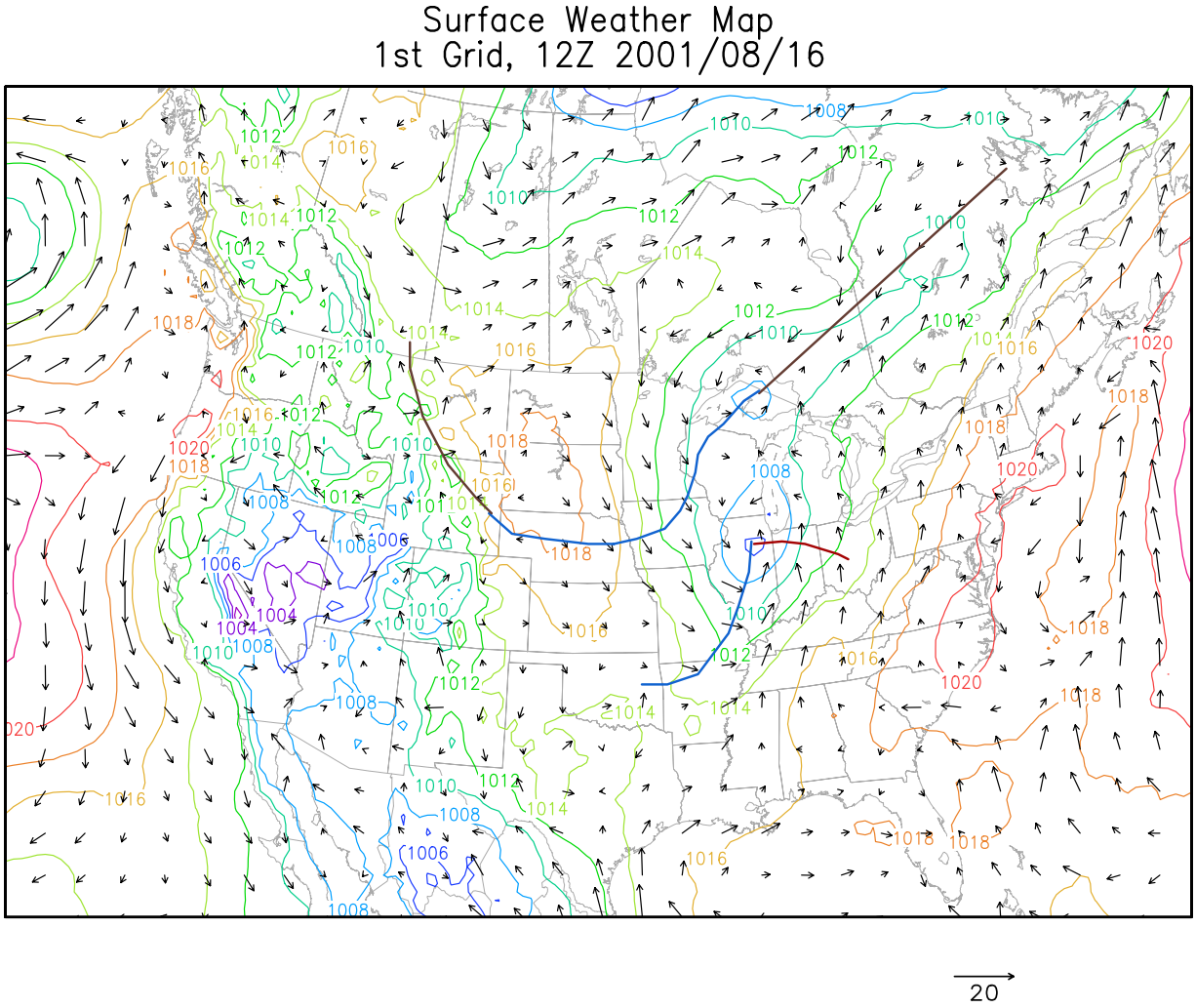


**Figure 1.** Surface weather map for the first grid, 1200 UT 16 August 2001. The surface pressure (unit is hPa) and wind vector (unit is m/s) data are based on Eta-40 km reanalysis data.

UT 17 August, 0.76 mm of rainfall was reported. Air temperature and pressure did not deviate significantly from the average diurnal cycle, but relative humidity dropped sharply after the rain. Radar detected precipitating rain clouds (not shown) after the wind direction shifted. Another low-pressure system was located to the south. That low came from the east side of the Rocky Mountains on 14 August and moved to the west bank of Lake Michigan on 16 August. Figure 1 shows the surface weather map at 1200 UT 16 August.

[11] This case was chosen because the data available during this time period had relatively few gaps, and because the [$CO_2$] rose more than 40 ppm at all the levels within 36 hours before the front arrived. The 40 ppm increase alone was more than twice the seasonal variation of that observed by flasks in the marine boundary layer in the Arctic, about five times of that in Hawaii, more than 20 times of that in the South Pacific Ocean, and about 40 times of that in the South Pole (http://www.cmdl.noaa.gov). Continental [$CO_2$] varies much more than in the marine boundary layer, and the $CO_2$ variability in the Northern Hemisphere is strongly influenced by the land biophysical processes. The front arrived in the early morning, and both the effect of convective boundary layer buildup (local scale) and the pressure systems (synoptic scale) made this case interesting. The response of the ecosystem to the weather was also one of the most important concerns in this study.

## 3. Model Description, Numerical Design, and Input Data

### 3.1. BRAMS and SiB

[12] The Regional Atmospheric Modeling System (RAMS [*Cotton et al.*, 2002; *Pielke et al.*, 1992]) was adopted as our base model. BRAMS (Brazilian RAMS [*Freitas et al.*, 2005]) was a new regional atmospheric model adapted from RAMS 5.04 with the Grell convection scheme and shallow convection scheme [*Grell et al.*, 1995] implemented in it. In this study, the land component of RAMS, LEAF (Land Ecosystem-Atmosphere Feedback [*Walko et al.*, 2000]), was replaced with SiB 2.5 [*Denning et al.*, 2003; *Nicholls et al.*, 2004]. We call the coupled model SiB-RAMS. In SiB 2.5, the Farquhar-Berry model is used to parameterize photosynthesis rate, and the Ball-Berry-Collatz equation links the photosynthesis rate with leaf-level conductance [*Collatz et al.*, 1991, 1992]. Know-

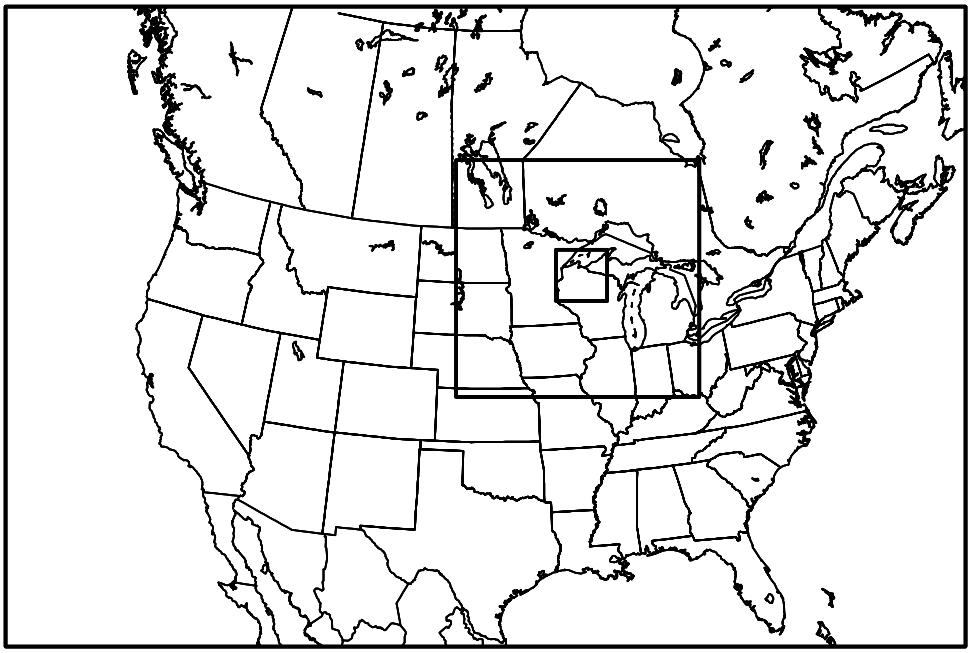

**Figure 2.** SiB-RAMS grids in this research.

ing the conductance, we can calculate the water, energy, and $CO_2$ exchange at the land surface simultaneously. The photosynthesis rate for each grid cell is scaled from the leaf-level to the canopy using satellite vegetation products. Using the Normalized Difference Vegetation Index (NDVI), SiB 2.5 estimates canopy-scale photosynthesis by assuming continuous vertical variation of leaf nitrogen, conductance, and photosynthesis following an exponential profile of time-mean photosynthetically active radiation (PAR). Each grid cell is divided into two patches: open water and dominant vegetation. The dominant vegetation patch takes into account bare soil fraction.

### 3.2. Model Configuration

[13] One coarse (the first) grid and two nested grids (the second and third) were used to achieve the goal of downscaling (see Figure 2 and Table 1). Grid 2 and Grid 3 had the WLEF site at the center. This two-way nesting method helped to simulate synoptic, mesoscale, and small-scale phenomena at the same time. This was especially valuable when both the local surface $CO_2$ budget and horizontal $CO_2$ advection were important for tower $CO_2$ observations during a frontal passage. Variable vertical grid spacing was used, ranging from 60 m near the surface to 1000 m well into the stratosphere.

[14] Table 2 shows the model configuration used in this study. The first grid adopted lateral boundary nudging to constrain the meteorological fields along the sides of the domain. For the first grid, zero gradient inflow and outflow boundary condition was used for tracer concentration, meaning the $CO_2$ inside the domain does not exchange with the outside. [$CO_2$] was initialized as 370 ppm homogeneously throughout the domain.

### 3.3. Input Data

[15] NCEP (National Center for Environmental Prediction) Eta model reanalysis data for AWIP Grid 212, which has 26 pressure levels and grid spacing of about 40 km, was extracted and reformatted for RAMS input. AWIP Grid 212 is a 40-km Lambert Conformal grid extending from roughly 20°N to 60°N, covering most of North America. The analyses of horizontal wind, temperature, geopotential height, and specific humidity were used as initial condition and boundary nudging weather data for our simulation.

[16] The anthropogenic $CO_2$ source, representing fossil fuel burning and cement manufacture, was prescribed from estimates by *Andres et al.* [1996]. They used the fossil fuel consumption of every country and the population density at every latitude and longitude degree to calculate $CO_2$ anthropogenic source flux for year 1995 (the latest available gridded data set). The emission strength was scaled to 1.112 times for August 2001 according to the monthly United States fossil fuel consumption record [*Marland et al.*, 2005]. Anthropogenic $CO_2$ was then emitted constantly on each grid point of the SiB-RAMS simulation domain at each time step.

[17] The climatological spatial distributions of monthly net sea-air $CO_2$ flux was estimated for the reference year of 1995 by *Takahashi et al.* [2002] on the basis of more than one million sea-air $CO_2$ partial pressure difference measurements and wind speed 10 m above the sea surface. The original grid increment of this data set was 5° by 4° and regridded (not interpolated) into 1° by 1°. Note that this sea-air $CO_2$ flux was not scaled to August 2001 as it was for the anthropogenic $CO_2$ source, because there was little information about its interannual variability.

**Table 1.** Grid Parameters

| | First Grid | Second Grid | Third Grid |
|---|---|---|---|
| Cell numbers | 150 × 100 | 150 × 150 | 182 × 182 |
| Grid spacing | 40 km × 40 km | 10 km × 10 km | 2 km × 2 km |
| Time step | 60 s | 30 s | 10 s |

**Table 2.** Model Options Used in This Study

| Category | Options Selected | References |
|---|---|---|
| Basic equations | nonhydrostatic, compressible | *Tripoli and Cotton* [1980] |
| Vertical coordinates | terrain-following sigma z | *Clark* [1977] and *Tripoli and Cotton* [1982] |
| Horizontal coordinates | oblique polar-stereographic projection | |
| Grid stagger and structure | Arakawa C grid, multiple nested grid (fixed) | *Arakawa and Lamb* [1977] |
| Time differencing | hybrid | |
| Microphysics | Bulk microphysics (single moment) | *Walko et al.* [1995] |
| Convective parameterization | Grell scheme with moisture convergence closure method for grid 1 and 2 | *Grell et al.* [1995] |
| Radiation | Harrington | *Harrington et al.* [1999, 2000] |
| Eddy diffusion | Mellor/Yamada scheme | *Mellor and Yamada* [1974, 1982] |
| Surface layer | SiB 2.5 and modified surface flux scheme | *Sellers et al.* [1996a, 1996b], *Holtslag and Boville* [1993], and *Louis* [1979] |

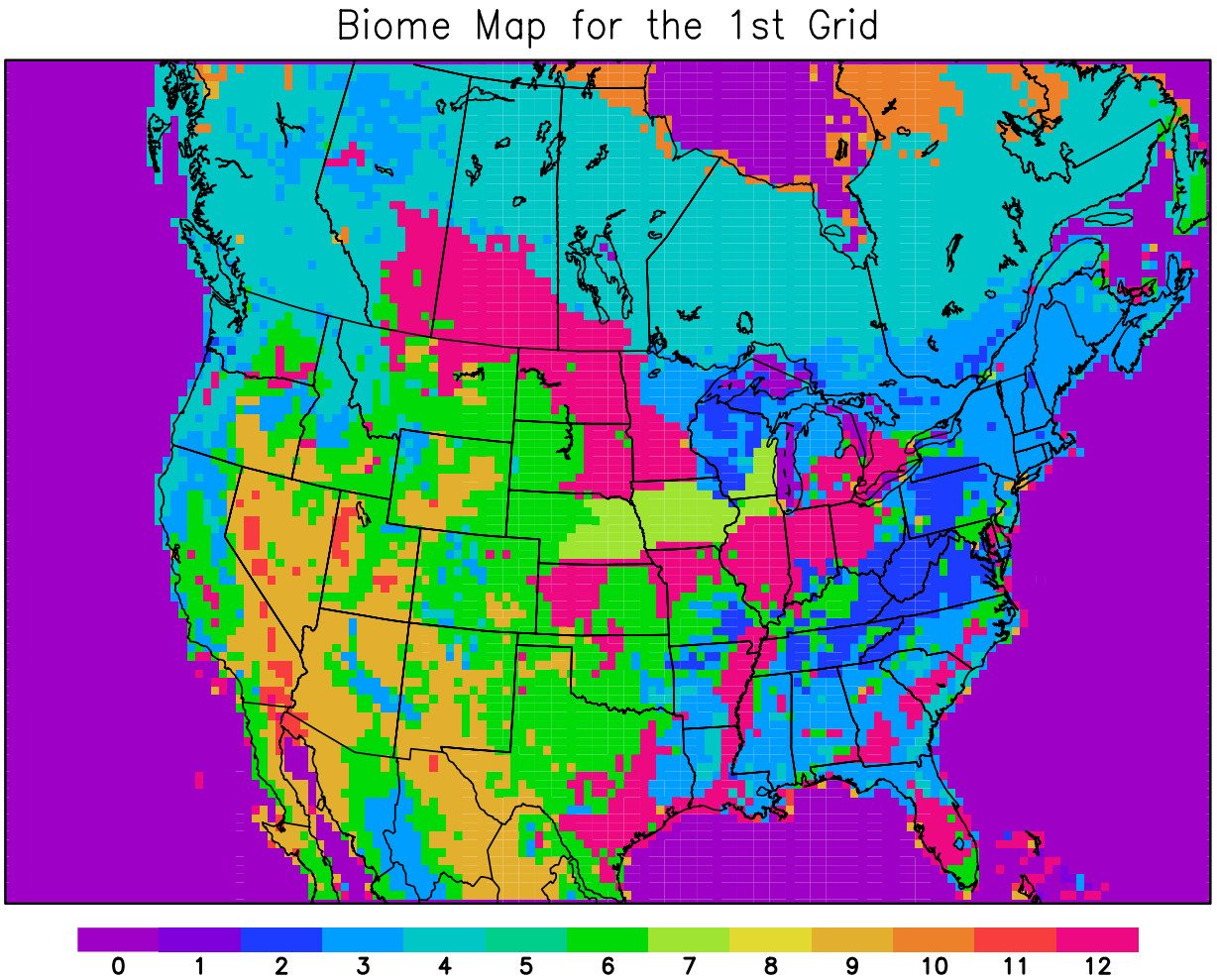


**Figure 3.** Biome map for the first grid. SiB 2.5 biome classes are as follow: 0, water body; 1, evergreen broadleaf tree (C3); 2, deciduous broadleaf tree (C3); 3, mixed woodland (C3); 4, evergreen needleleaf tree (C3); 5, deciduous needleleaf tree (C3); 6, short grass (C4); 7, maize (C4); 8, not used; 9, deciduous shrub (C3); 10, tundra (C3); 11, desert/bare soil; 12, C3 crop/mixed farming/C3 grassland (C3).

### 3.4. Soils, Vegetation Cover, and NDVI

[18] The soil map for SiB-RAMS was a product of the International Geosphere-Biosphere Programme (IGBP [*Global Soil Data Task*, 2000]). The original data was a soil type map of %sand/%clay/%silt values with 5′ (~10 km) resolution. The data were then binned into soil classes [*Sellers et al.*, 1996b].

[19] *Hansen et al.* [2000] have developed a reproducible biome classification algorithm and practiced it on the NASA/NOAA Pathfinder Land (PAL) data set with the spatial resolution of 1 km from 1981 to 1994. Their method, however, did not distinguish C3 crops, C4 crops, and C4 grassland from one another. *Leff et al.* [2004] have synthesized satellite-derived land cover data and agricultural census data to produce global data sets for the distribution of 18 major crops across the world. The resulting data were representative of the early 1990s and had the spatial resolution of 5 min (close to10 km). The crop fraction map from *Leff et al.* [2004] was used to further discriminate biome classes from *Hansen et al.* [2000]. The biome classes were converted to SiB classes accordingly. Figure 3 shows our new biome map.

[20] The Normalized Difference Vegetation Index (NDVI) was from the French satellite SPOT-4 (Systeme Probatoire d'Observation de la Terre polar orbiting satellite; United States Department of Agriculture/Foreign Agriculture Service and Global Inventory Modeling and Mapping Studies) data set with a footprint of 1 km. The SPOT NDVI data were 10-day maximum value composites. Any points that were flagged because of ice/snow or cloud were filled by interpolation of the closest values in time in that pixel.

### 3.5. Model Spin-Up and SiB Initialization

[21] To initialize soil moisture, respirable carbon, and other variables, we ran SiB 2.5 offline on a global $1^\circ \times 1^\circ$ grid using NCEP/NCAR reanalysis driver data from the year 1991 to the year 2001. After doing so, we interpolated the output into our SiB-RAMS grid points in the coupled model for surface variables, such as soil water content fraction, soil temperature, canopy space temperature, snow depth, canopy temperature. The online model was then "trained" for another 10 days (1–10 August 2001) before the period of interest. SiB has three layers for soil moisture and seven layers for soil temperature. The first (top) layer is exposed to the atmosphere and exchange energy, water, and $CO_2$ with it. Except for the soil moisture and temperature in and below the second layer, all the SiB 2.5 variables adjusted to the model weather within the 10 days. SiB 2.5 assumes a balanced annual carbon budget over land; that is, aboveground net assimilation equals ground respiration over a period of 1 year [*Denning et al.*, 1996]. This is reasonable because the soil carbon pool changes over time very slowly relative to the short period of our simulations. The neutral annual carbon budget constraint for each SiB-RAMS grid cell was given based upon the offline SiB 10-year spin-up results from the closest grid cell that occupied the same biome type. The constraint asserts itself a balanced carbon budget for the whole year, including summer (photosynthesis is stronger) and winter (photosynthesis is weaker); hence, for this summer frontal case, soil respiration will have smaller magnitude than vegetation net photosynthesis. Note that the land surface initialization and neutral annual carbon information for SiB-RAMS (horizontal resolution is listed in Table 1) was given from 1° resolution offline SiB run.

## 4. Results and Discussion

### 4.1. Regional Analysis

#### 4.1.1. Model Evaluation of Near-Surface Meteorology: NARR Versus Experiment

[22] Figure 4 shows the difference of temperature and water vapor mixing ratio at 29.3 m above the ground (the first level in the model), and wind field at 396 m between North American Regional Reanalysis (NARR [*Mesinger et al.*, 2006]) data and SiB-RAMS simulation at 1200 UT 16 August 2001. Sea surface temperature (SST) determined the nearshore and offshore near-surface air temperature and water vapor mixing ratio. The climatological SST was apparently too large in this case, and it can be improved by using satellite derived nonclimatological SST (e.g., NCEP Reynolds Optimally Interpolated Sea Surface Temperature Data Sets; http://podaac.jpl.nasa.gov/sst) in the future. In general, air temperature was underestimated except southwestern United States and offshore west coast. Our simulated water vapor mixing ratio was more problematic and was probably associated with the biome types. The forest and woodland (eastern United States and Canada) usually had mixing ratio overestimated, while the shrub had it underestimated.

[23] As for wind field at 396 m, our model shows more northerly wind in the northern Great Plains and stronger convergence zone stretching from Texas to Lake Erie. The stronger northerly wind in our model at 1200 UT 16 August 2001 explained part of the reason why the modeled $[CO_2]$ at WLEF started decreasing early, which will be shown in section 4.1.3.

[24] Figure 5 (top) shows the spatial correlation coefficient (CC) time series of temperature and water vapor mixing ratio at 29.3 m and zonal and horizontal wind at 396 m of the first grid. NARR data time interval is 3 hours. Temperature CC is usually between 0.6 and 0.75, while water vapor mixing ratio CC varies between 0.36 and 0.78. Water vapor mixing ratio is especially lower from 14 to 16 August, which is the time window when the cold front moved across the central and eastern United States. Temperature and water vapor CC fluctuate in the opposite throughout the comparison period. This clearly points to the land surface energy partition. When the outgoing energy is more in the form of sensible heat flux (less in latent heat flux), the first atmospheric level has higher temperature. When the outgoing energy is more in the form of latent heat flux (less in the sensible heat flux), the first level has more humidity. The outgoing surface energy in our coupled model shows a different way of partition in the diurnal cycle against NARR.

[25] Figure 5 (bottom) shows the CC of zonal and meridional wind speed. Our simulated meridional wind shows good agreement with NARR, although the CC is smaller on 16 and 17 August. As for the zonal wind, the CC

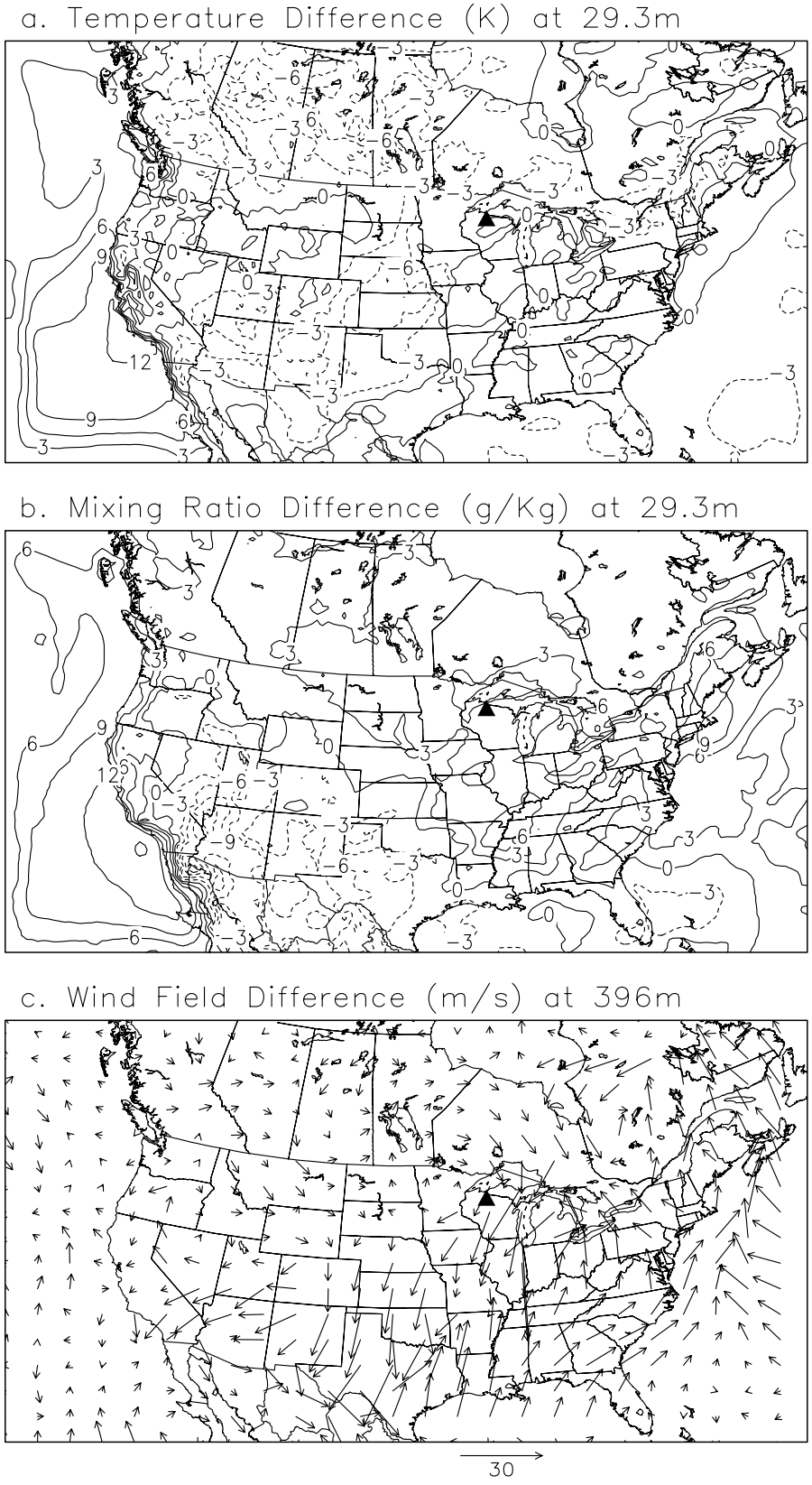


**Figure 4.** Difference of (a) temperature at 29.3 m, (b) water vapor mixing ratio at 29.3 m, and (c) wind field at 396 m, between the simulation results and NARR at 1200 UT 16 August 2001.

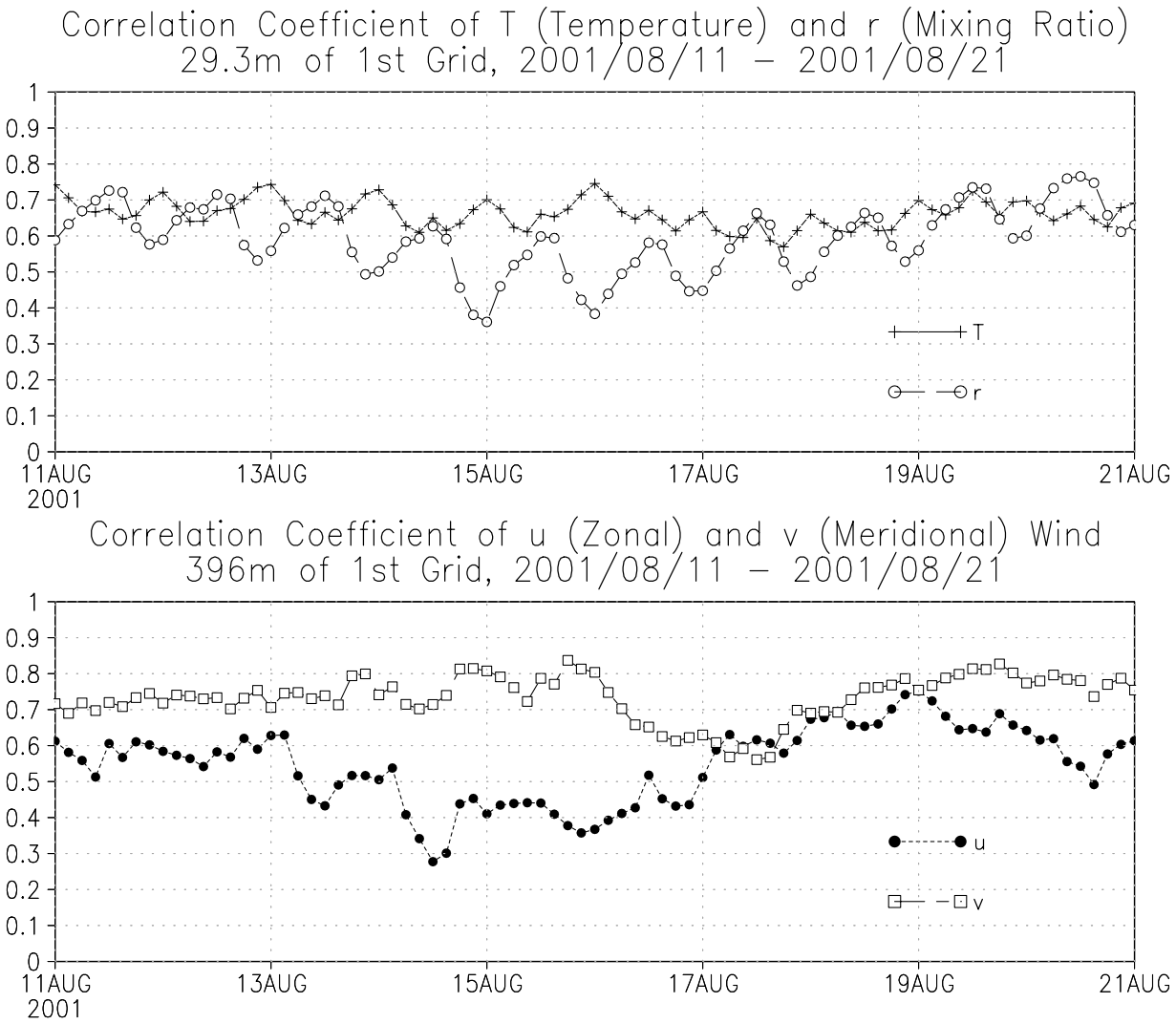


**Figure 5.** (top) Two-dimensional spatial correlation coefficients time series of temperature and water vapor mixing ratio at 29.3 m and (bottom) zonal and meridional wind speed at 396 m for the period of 11–21 August 2001.

varies from 0.3 to 0.75. The spatial pattern of zonal wind between 13 and 16 August was not well simulated.

#### 4.1.2. Synoptic $CO_2$ Transport in the Model

[26] Figure 6 shows a 12-hourly mean surface $CO_2$ flux and a [$CO_2$] snapshot on the last hour of the averaging period at 396 m above the ground. In the model, there was usually a systematic low-[$CO_2$] region in the northern Great Plains, covering Wisconsin, Illinois, Minnesota, Iowa, South Dakota, Nebraska, etc. (not shown). Air from that region (with concentration as low as 355 ppm) was advected to the northeast across the Lake Superior at 1200 UT 15 August and earlier. We can see from Figure 6 (left) that even during the daytime of 15 August, southern Texas was a significant source of $CO_2$ into the atmosphere and Oklahoma was a weak source. During the nighttime, strong $CO_2$ emissions were simulated over parts of the southeastern United States. The southerly wind advected this high-[$CO_2$] air northward, over northern Oklahoma and southern Kansas (as shown at 1200 UT 15 August), and thus a high-[$CO_2$] zone was located to the north (Oklahoma and Kansas) of the strong source (Texas), as shown in Figure 6 (right). There was a weak daytime $CO_2$ source in Iowa on 15 August as a result of reduced incoming shortwave radiation associated with stormy weather there. When a cyclone formed on 15 August and brought the $CO_2$-rich air into its center, the shape of high-[$CO_2$] air mass also changed accordingly. Northerly wind dominated in the northern part of the Great Plains and southerly wind dominated in the southern part of this region. A convergence zone in the Great Plains gradually formed and carried $CO_2$-rich air to Wisconsin at 0000 UT 16 August. The major convergence zone was aligned northeast to southwest across the entire southern Great Plains. In the meantime, ecosystems in southern Texas acted as a strong net source of $CO_2$, because of the reduced vegetation uptake and strengthened soil respiration associated with the very hot weather there (discussed below), and winds advected this relatively high-[$CO_2$] air to the east coast (0000 UT 17 August).

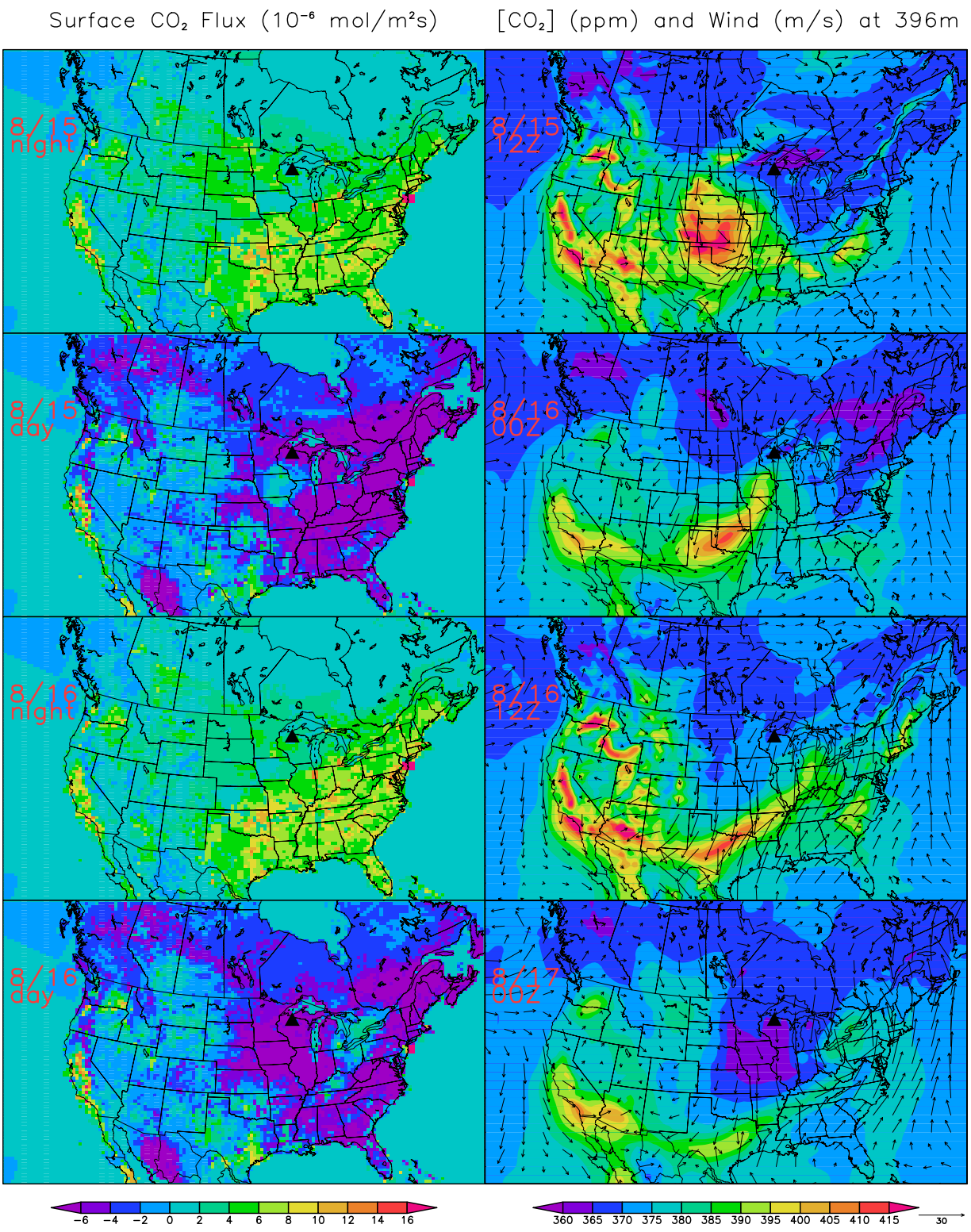


**Figure 6.** (left) Model 12-hourly mean surface $CO_2$ flux, including SiB calculated NEEC and anthropogenic $CO_2$ source, and (right) $CO_2$ spatial distribution with wind vector at 396 m above the ground. The word "day" used in the figure means that it is 12-hour average while most of the conterminous U.S. soil is at daytime (1300–2400 UT), and the word "night" is for nighttime (0100–1200 UT). Time frame is 15–16 August. Figure 6 (right) shows snapshots at the last hour of the averaging period in the left pane. The solid triangles indicate the position of the WLEF tower.

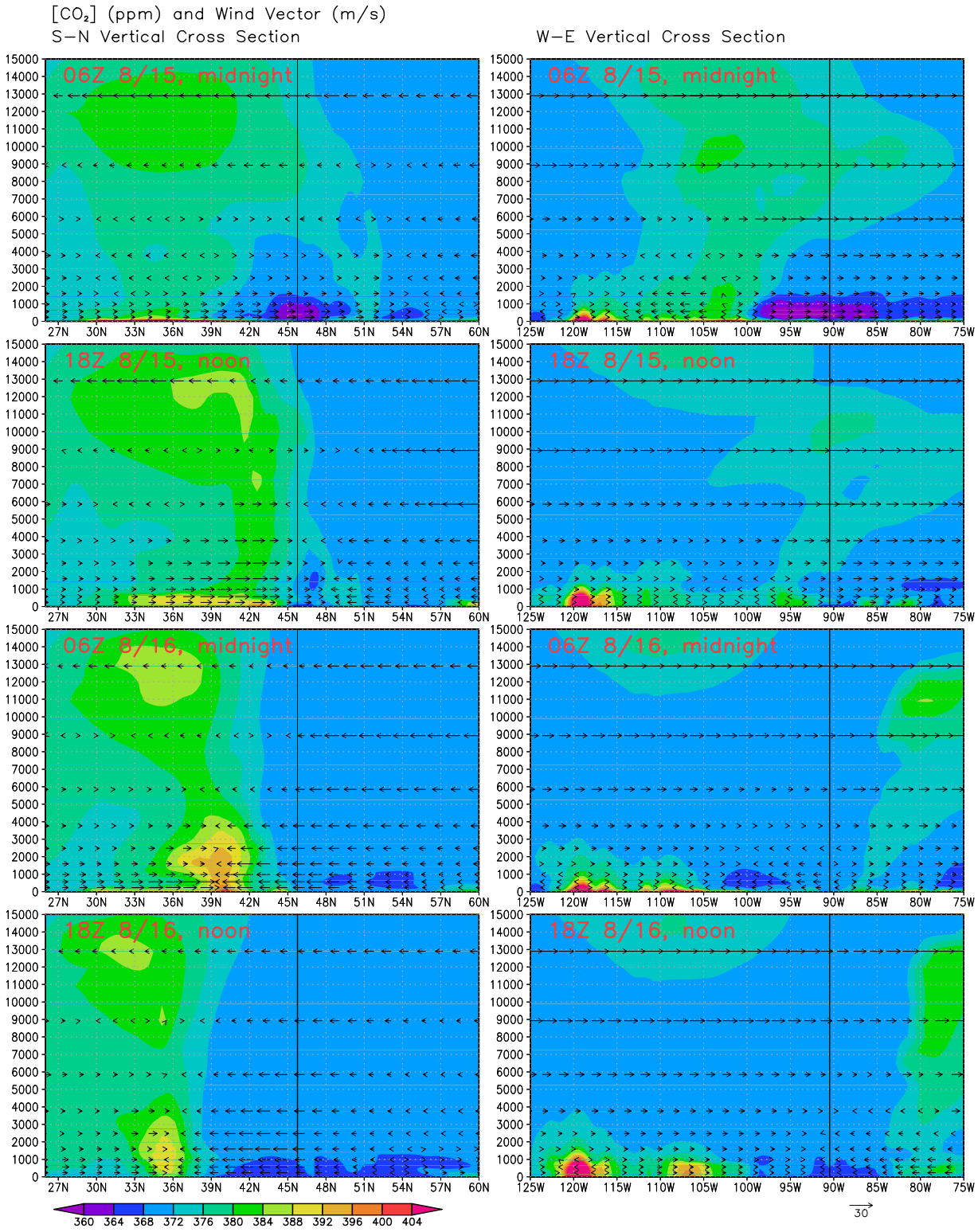


**Figure 7.** $CO_2$ vertical profile and wind vector (left) for the south-north direction and (right) for the west-east direction. Time frame is for 15–16 August. Vertical lines indicate the position of the WLEF tower.

[27] Figure 7 (left) displays the north-south $CO_2$ vertical cross sections from the ground surface to 15,000 m for the first grid, at the longitude of the WLEF tower, together with wind vectors and their temporal evolution. The vertical solid black lines denote the location of the WLEF tower. During the nighttime of 15 August, $CO_2$ started to accumulate near the surface in a wide area from 30 to 42°N (0600 UT 15 August); the wind transported $CO_2$ northward in the

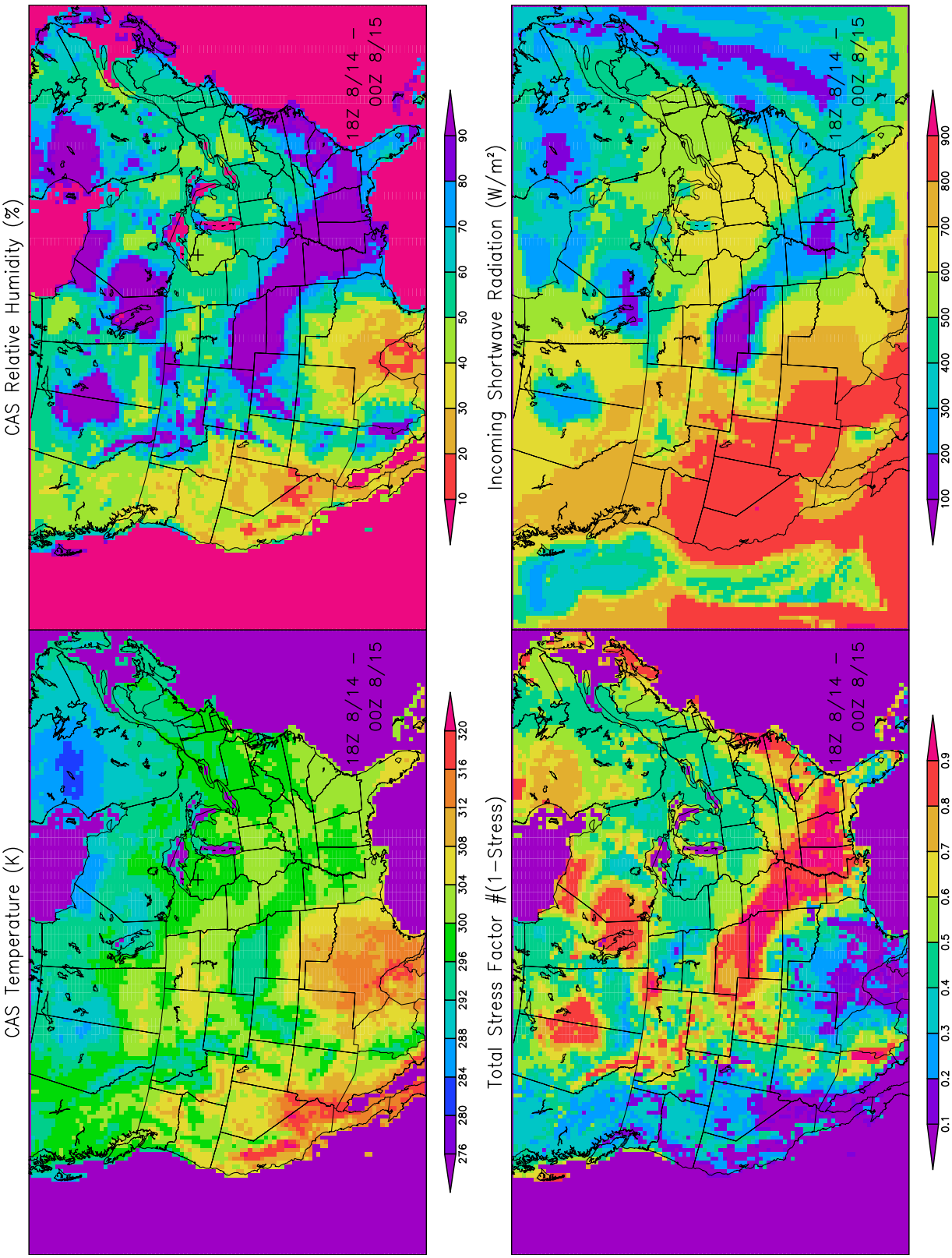


**Figure 8.** The 6-hour mean CAS temperature, CAS relative humidity, total stress factor for photosynthesis, and incoming solar radiation for the first grid for the period from 1800 UT 14 August to 0000 UT 15 August.

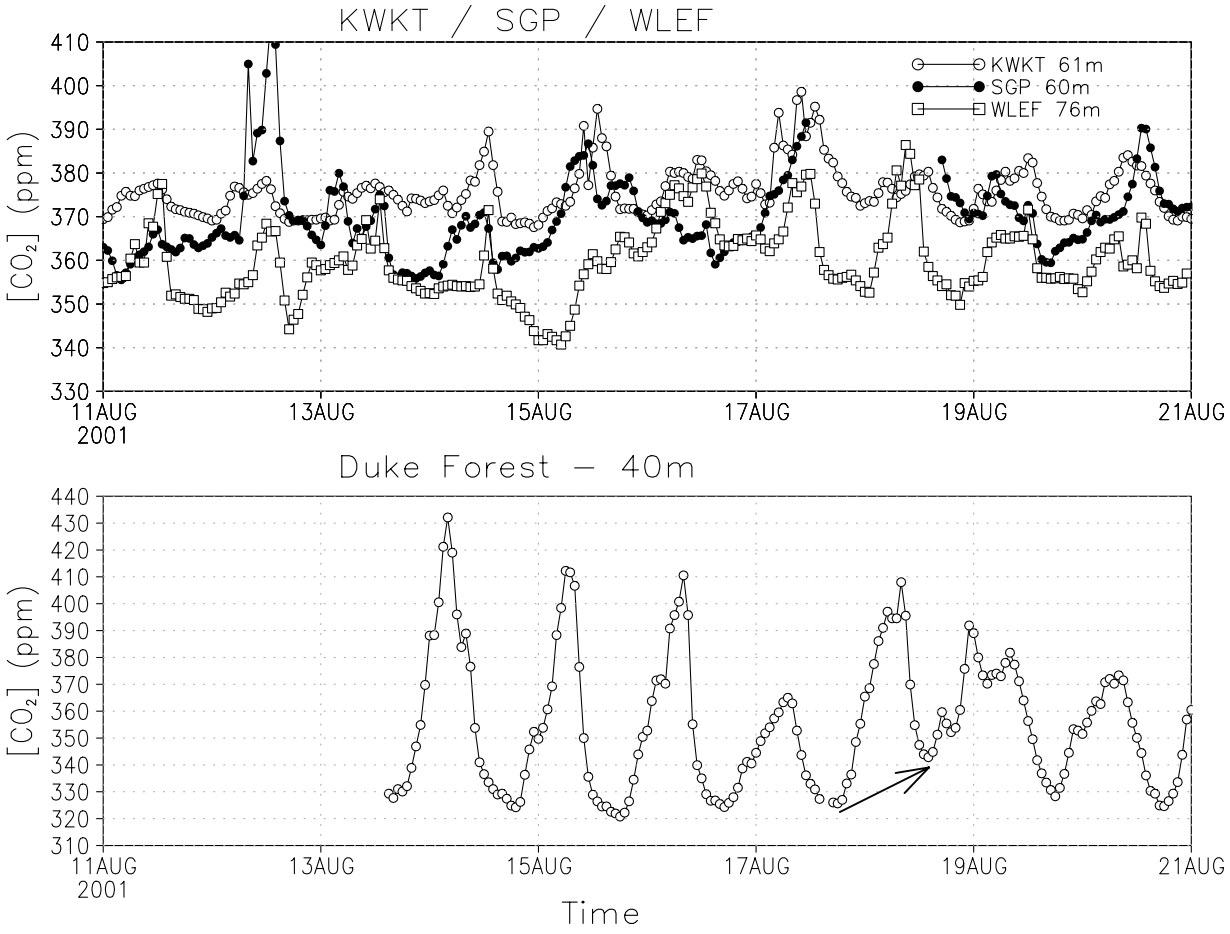


**Figure 9.** [$CO_2$] time series between 11 and 21 August for the four different sites: KWKT (61 m), SGP (60 m), WLEF (76 m), and Duke Forest (40 m).

lower levels (below 2000 m), and the low-[$CO_2$] air to the south of WLEF moved across the tower. A convergence zone near the surface was present at 48°N at 1800 UT 15 August, where the wind direction reversed. The convergence zone then moved slowly to the south at first (0600 UT 16 August). $CO_2$ was pushed upward and a little to the south of the convergence zone. Anomalies aloft were due to cumulus convection associated with this strong surface convergence. In the model, the leading edge of the high-[$CO_2$] zone reached the WLEF site and resided there for a very short time (1800 UT 15 August to 0000 UT 16 August). The $CO_2$-rich air around WLEF was replaced by the air from the north immediately afterward.

[28] Figure 7 (right) shows the $CO_2$ anomalies in the east-west direction at the latitude of the WLEF tower. The high-[$CO_2$] zone was located to the west of the Great Plains when the cyclone on 15 August formed. At 0600 UT 15 August, a divergence zone formed around 104°W, and the high-[$CO_2$] air moved west while the low-[$CO_2$] air traveled east. The eastern branch passed the WLEF tower about the same time as from the N–S view. After 0600 UT 16 August, another positive anomaly gradually formed between 105°W and 110°W, which traveled east, while to the east of 120°W $CO_2$ was advected in from the west coast.

[29] Figure 7 shows that $CO_2$ variability is significant in the vertical direction. Traditionally, $CO_2$ is observed near surface up to 500 m above the ground (e.g., AmeriFlux), and its vertical distribution is inevitably missed except in the intense aircraft observations. Note that model vertical transport did not only rely on resolved vertical wind but also on convection parameterization.

#### 4.1.3. Regional $CO_2$ Sources and Sinks Pertinent to the Regional Weather Variation

[30] Ecosystems in southern Texas were a strong source of $CO_2$ during the daytime on 14 and 15 August in our simulation. Figure 8 shows canopy air space (CAS) temperature, CAS relative humidity, total stress factor for photosynthesis, and incoming shortwave radiation for the first grid at 1800 UT 14 August to 0000 UT 15 August (afternoon for most of domain). Southern Texas was extremely hot at that time, while CAS relative humidity was very low (note that the color table is reversed). Simulated physiological stress, primarily due to high leaf temperature and low relative humidity (but not to dry soils), led to photosynthesis in some areas being reduced below 10% of its potential value. Ground surface temperature at that time was very high in Texas and Oklahoma (above 40°C, not shown). High soil temperature produced enhanced simulated heterotrophic respiration, resulting in an additional efflux of $CO_2$ into the atmosphere. Extreme values of CAS temperatures present in California and Texas continued for two days until northerly winds brought cool air down to north-

ern Texas on 17 August (refer to 0000 UT 17 August in Figure 6 (right)).

[31] There was also a cool and humid area with clouds and rain extending from the lower Mississippi basin to Nebraska. The resulting reduction in surface shortwave radiation over Nebraska at that time (Figure 8, bottom right) depressed daytime uptake of $CO_2$ to near zero in the afternoon of 14 August. This zone of reduced shortwave radiation and NEEC then propagated to the east.

#### 4.1.4. Supportive Evidence From Surface Weather Stations and AmeriFlux Towers

##### 4.1.4.1. Hot Weather in Oklahoma and Texas

[32] Observed daily maximum temperatures in Oklahoma and Texas on 14 and 15 August from station data confirmed the existence of heat waves. Austin (30.3°N, 97.7°W, elevation: 189.3 m), Dallas-Fort Worth (32.9°N, 97.017°W, elevation: 170.7 m), Laredo (27.55°N, 99.467°W, elevation: 155 m), Oklahoma (35.383°N, 97.6°W, elevation: 397.5 m) and San Antonio (29.533°N, 98.467°W, elevation: 246.6 m) registered maximum screen height air temperature as high as 37°C, 37°C, 38°C, 35°C, and 37°C, respectively. Also, the lowest relative humidity for those stations on 14 and 15 August was 34%, 29%, 23%, 35%, and 25%, respectively.

##### 4.1.4.2. $CO_2$ Data From KWKT (61 m), SGP (60 m), WLEF (30 and 76 m), and Duke Forest (40 m)

[33] We examined available records of observed simulated $[CO_2]$ to further investigate the synoptic-scale variations simulated by the model. Figure 9 shows $[CO_2]$ from four different sites in the same time frame. The ARM/SGP (Atmospheric Radiation Measurement Program/Southern Great Plains) site is located in Lamont, Oklahoma. The surrounding vegetation type is winter wheat, some pasture, and summer crops [*Sheridan et al.*, 2001]. The KWKT site has a 505-m tall tower near the town of Moody in central Texas. The region is within a strong east-west moisture gradient, and the local land use is dominated by cattle grazing. The Duke Forest hardwoods site is in North Carolina, with the hardwood trees 90 to 110 years old surrounding it [*Katul et al.*, 2003]. The four sites do not have the same measurement heights, which affects the amplitude of the diurnal cycle because of nocturnal stratification. The SGP site had a very high $[CO_2]$ spike on 12 August, which might be related to its shallow nighttime stable layer. The $[CO_2]$ at SGP showed a maximum value on 15 August, which led the maximum at WLEF on 16 August by 26 hours. On 15 August the difference between SGP and WLEF was as large as 38 ppm. The observations therefore confirm a SW–NE gradient of several 10 s of ppm as simulated by the model (Figure 6). On 16 August, the model simulated cooling in Oklahoma associated with northerly winds, with a resulting recovery of photosynthesis and decreased respiration. This is consistent with the decreasing trend of the observed $[CO_2]$ at SGP on 16 August in Figure 9 (top). Duke Forest did not detect strong $CO_2$ signals that were produced in Texas and traveled with the front, although it showed three peak values on 18 August, which matched the timing of the simulated positive $CO_2$ anomaly transported to the east coast in the model. We can see that during the period of 13 to 20 August, only on 18 August Duke Forest had an elevated minimum $CO_2$ mixing ratio.

[34] Figure 10 shows NEEC from the SGP site and the CSP (Carbon Sequestration Program) site, located in Mead Nebraska [*Verma et al.*, 2005]. The vegetation surrounding the CSP site 3 is rainfed maize. The vegetation around SGP (wheat, pasture, and summer crops) had a photosynthesis capacity of more than 12 $\mu$mol $m^{-2}$ $s^{-1}$ in the period of interest. However, on 13 and 14 August, the typical daytime observed NEEC was only 2–5 $\mu$mol $m^{-2}$ $s^{-1}$. On 15 August, only one data point was more than 3 $\mu$mol $m^{-2}$ $s^{-1}$. This shows that the vegetation around the SGP site was stressed by the high temperatures and the relatively low humidity, consistent with the simulation (Figure 8). We do not have any NEEC observations in Texas, so the stress condition of the model cannot be evaluated. The observed NEEC at the CSP site decreased during the daytime of 14 and 15 August, although the decrease was not as significant as in the model. The site measurements indicated reduced surface shortwave radiation (not shown) as well. The observations thus confirm the existence of a reduced photosynthesis rate in Oklahoma associated with hot dry weather and in Nebraska associated with reduced incoming solar radiation.

### 4.2. Local Analysis

#### 4.2.1. Near-Surface Meteorology at WLEF

[35] A comparison of near-surface meteorological fields between the observations and the SiB-RAMS simulations was performed for the period of 11 August 2001 through 20 August 2001. Some of the model vertical layers were set as close to the tower measuring levels as possible. Figure 11a shows the comparison of air temperature at 30 m. The model captured the variations with the exception of the daytime of 15 August, which was a cool and cloudy day. The low daytime temperature on 15 August was the result from the frontal passage. Yet, the model did not capture the decreasing magnitude well. The model everyday minimum temperature lagged the observations by 3–4 hours on 11, 13, and 14 August. For 11–14 August, minimum temperature was overestimated. The observed temperature started rising from 12 to 14 August and suddenly dropped during the daytime of 15 August. On 15 August the nighttime temperature at the 30-m level of the WLEF tower was highest during the period of interest, and its variation on the following day was the smallest. Cloudy sky conditions were responsible for the small temperature variation on late 15 August as well as the entire day of 16 August. Nearby weather station data (Phillips, Wisconsin; 45.7°N, −90.4°W; about 25 km south of the WLEF tower) showed overcast sky conditions from 1100 UT 15 August to 1000 UT 17 August, with only a few other sky conditions in between (1 "CLR", 3 "SCT", and 2 "BKN"; in other words, one clear sky, three 3/8–4/8 of cloud cover, and two 5/8–7/8 of cloud cover). High nighttime temperature might explain why the nighttime respiration on 15 and 16 August was a little higher than usual, which is shown in Figure 12.

[36] The water vapor mixing ratio from the model simulated the increasing trend from 13 August to late 15 August (Figure 11b); however, the model had the mixing ratio drop on 12 August earlier, overestimated it on 15 August, and missed the peak on late 16 August.

[37] Figures 11c and 11d compare simulated and observed wind speed and wind direction at 396 m. Figure 11c shows

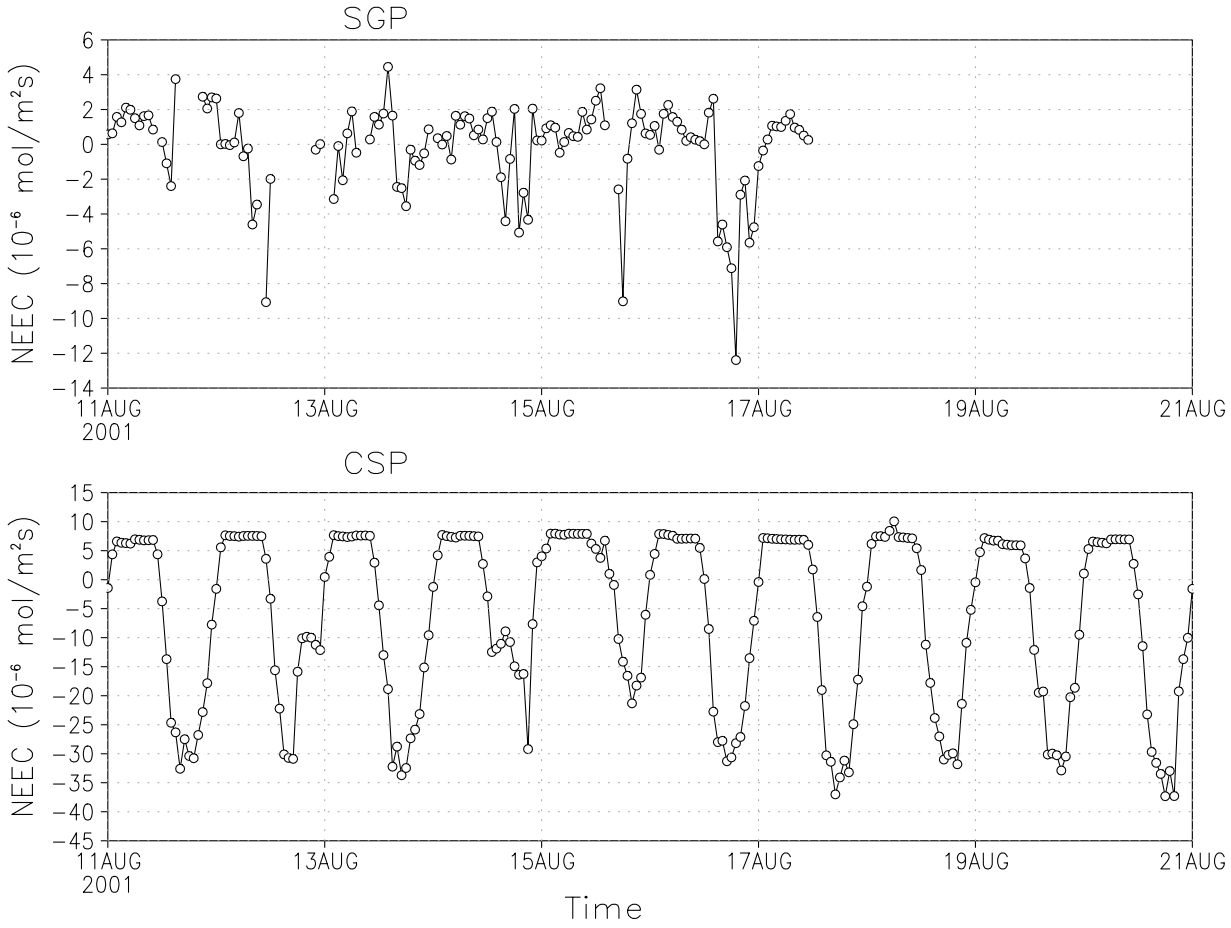


**Figure 10.** NEEC for the SGP site and the CSP 3 (rainfed maze) site.

that overall the model wind speed matches the tower observation reasonably well. However, the wind speed variation on 16 and 17 August was out of phase (anticorrelated), and the spike on 12 August was overestimated in the model. The simulated wind direction also matched the observations well in general, but there were mismatches on 16 and 17 August. The observations showed the wind direction changed from the southwest, turning clockwise to the north on 16 August, and counterclockwise back to the southwest on 17 August; the simulation showed the wind direction changed from the northeast to the north on 16 August, and to the southwest on 17 August. The mismatched wind directions might affect the simulation of [$CO_2$] mixing ratio variation at 396 m of the WLEF tower. The timing of the frontal passage was apparently not simulated well. The weak cold front that was supposed to be located on Lake Superior moved too fast and resided further to the east. The location of the low center determined the wind speed and wind direction (Figure 6).

#### 4.2.2. $CO_2$ Data at WLEF

[38] Figure 12a displays the comparison of the net ecosystem exchange of carbon (NEEC) between the simulation and the observations. We can see that the pattern in the model output was mostly due to the diurnal cycle, while the observations had more hour-to-hour variations. That is because the eddy covariance measurements reflect a limited sample of the turbulent transport, thus have inherent turbulent sampling uncertainty [*Lenschow et al.*, 1994; *Berger et al.*, 2001], whereas the simulation represents the areally averaged ecosystem-atmosphere exchange and varies only in response to environmental forcing. The observed nighttime NEEC on 15 and 16 August was higher than usual, and all the daytime NEEC observations on 15 August were positive ($CO_2$ source) with a few points missing. The observed daytime uptake (negative NEEC) on 16 August was comparatively weaker. The model simulated the average amplitude of the diurnal cycle in NEEC about right, but it had less day-to-day variation than the observations.

[39] Figure 12b shows [$CO_2$] anomalies at 29.3 m for the model and 30 m for the observations. The model correctly simulated the timing of diurnal cycle but underestimated the day-to-day variability. The model showed a weaker diurnal cycle on 15 and 16 August, whereas the observation increased in a uniform trend between early 15 August and 1300 UT 16 August. At this level, the concentration was strongly influenced by the local NEEC and the diurnal variation of vertical stratification of the atmospheric boundary layer.

[40] A comparison of [$CO_2$] between the model output and the observation at 396 m is shown in Figure 12c. There were three significant events in these observations. The first was the [$CO_2$] decrease from 11 August to early 12 August then jump on 12 August; the second was the strong dip on 15 August, and the third was the spike on 16 August. The

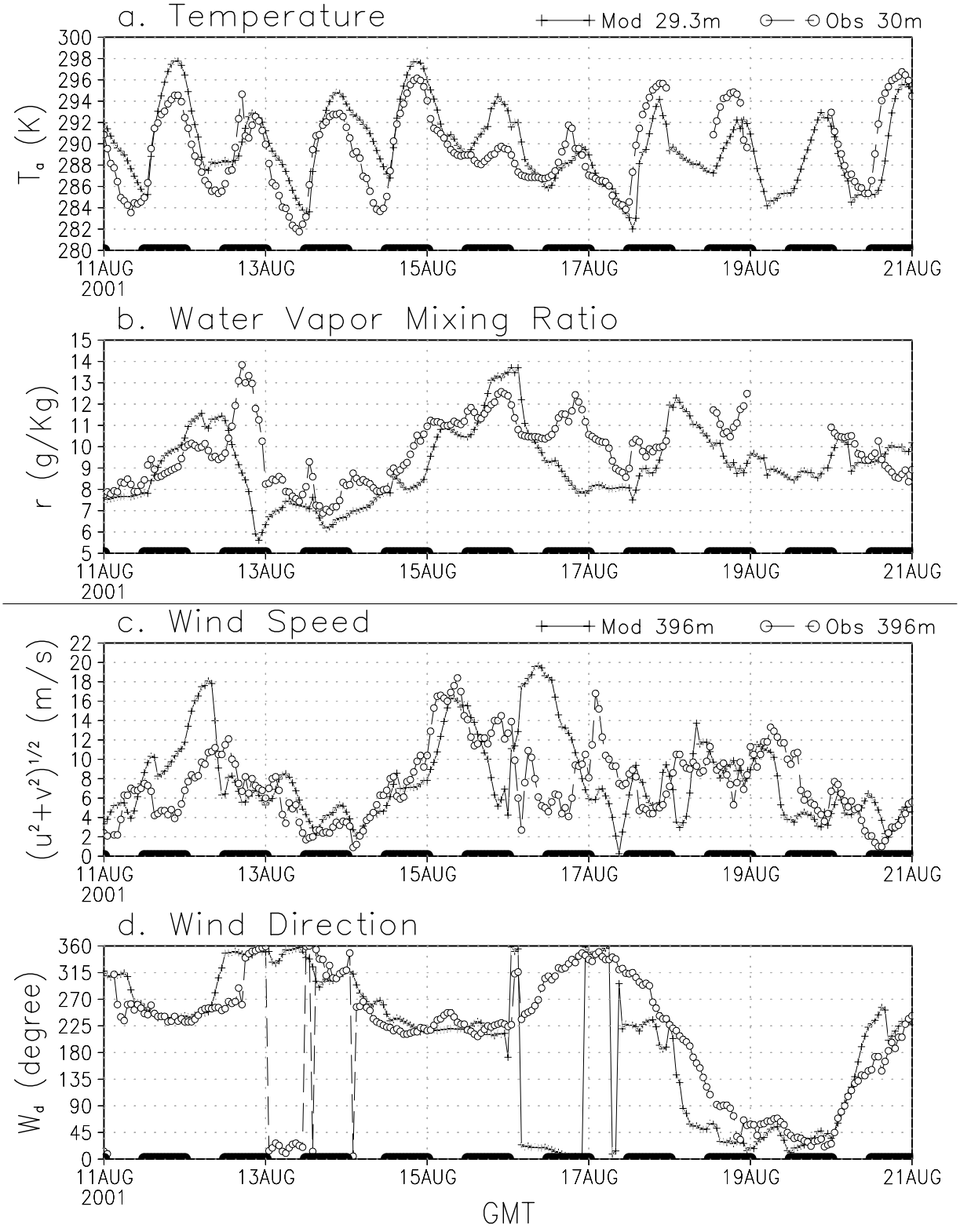


**Figure 11.** Comparison of (a) air temperature and (b) water vapor mixing ratio between tower observation (30 m) and model simulation (29.3 m) and comparison of (c) wind speed and (d) wind direction at 396 m. The model result is from the cell of the third grid (the inner grid) nearest to the WLEF tower. The thick black line on the *x* axis denotes the daytime.

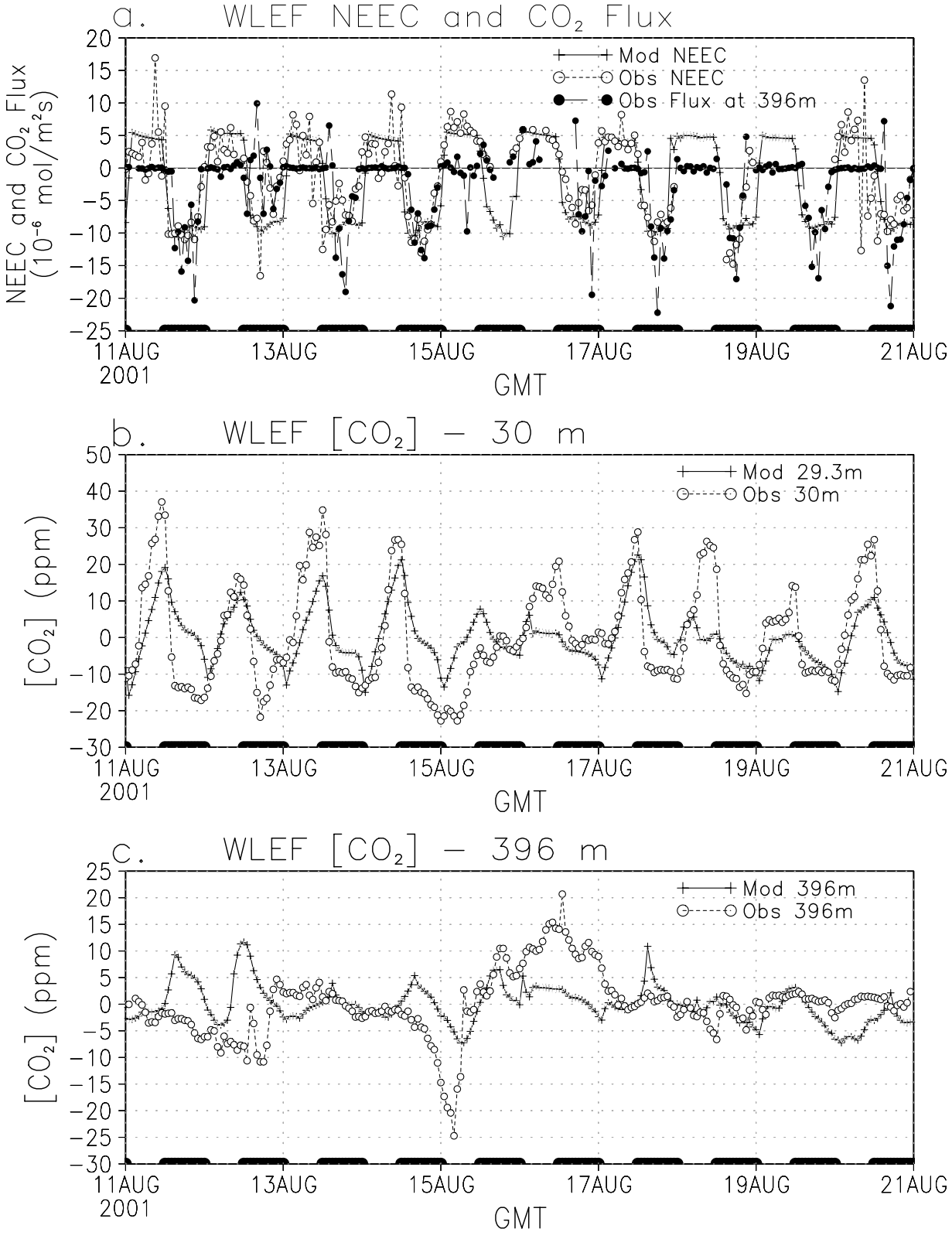


**Figure 12.** (a) Comparison of NEEC between tower observation and model simulation, together with the $CO_2$ flux at 396 m, and the comparison of (b) [$CO_2$] at the lowest level and (c) [$CO_2$] at the highest level of the tower. The thick black line on *x* axis denotes the daytime.

anomalies were as large as 20 ppm. [$CO_2$] changed more swiftly on 12 August in the observations. The model also had the decrease on late 11 August and early 12 August, but it was more sudden. The model had a weaker dip as shown on 15 August. This large dip was evidently due to the horizontal advection of low-[$CO_2$] air, because it happened at night when the local ecosystem forcing was limited to respiration releasing $CO_2$ into the air. The maximum value at 1300 UT 16 August was not well captured, and we suspect the problem was associated the model NEEC on 15 and 16 August as described above.

[41] The model underestimated the strong prefrontal decrease in $CO_2$ mixing ratio (more than 20 ppm for 244 m and 396 m) at the WLEF tower on 15 August. The cause for this large dip must have been horizontal advection of low-[$CO_2$] air, because the minimum value happened at 0400 UT, after the $CO_2$ mixing ratio at lower levels stopped decreasing and NEEC was positive. The eddy covariance (turbulent) flux at 396 m was very close to zero at night (Figure 12a), even when the NEEC was large. This means that the respiration signal from the ecosystem could not reach the 396 m because of the shallow stable nocturnal boundary layer. In this situation, NEEC is measured by the rate of change of the column-integrated mixing ratio [*Yi et al.*, 2000; *Davis et al.*, 2003]. *Wang* [2005] also practiced the concept of vertical divergence flux to estimate layer-average [$CO_2$] for the same tower and showed that local NEEC alone was not sufficient to explain [$CO_2$] variation, especially during a synoptic system event.

### 4.3. Discussion About Data Assimilation Using WLEF Observations

[42] The map in Figure 6 indicated that the large horizontal gradient of $CO_2$ was present in the domain (purple to red = $\sim$50 ppm). However, the extreme temporal variation seen in the WLEF observations was not well captured in our model. The wind field error assessment in Figure 4 shows that the simulated northerly wind started to dominate in the northern part of the Great Plains earlier than in NARR. This might lead to the early drawdown of [$CO_2$] before 1300 UT 16 August 2001 at the WLEF tower.

[43] When comparing a regional model simulation with observations at a single point, the comparison can be adversely affected by small simulation errors in both space and time; this is a critical problem that must be addressed if continental $CO_2$ data is to be used for data assimilation. In this case study, for example, if we assume that the transport is accurately simulated, the fluxes will then be inappropriately adjusted to compensate for transport errors. Therefore we must either well simulate synoptic events or filter out the signals from them, before we practice $CO_2$ data assimilation and use the coupled model to locate regional $CO_2$ source and sink.

## 5. Conclusion

[44] We employed a fully coupled atmosphere-biosphere model to study the $CO_2$ variation signals related to a frontal event in August 2001. The model treated $CO_2$ as a free variable and also allowed it to determine photosynthesis rate. SiB-RAMS reproduced many aspects of biospheric and meteorological features, including daily cycles of NEEC, temperature, air pressure, and wind direction during the period of interest (0000 UT 11 August 2001 to 0000 UT 21 August 2001); however, the timing and the location of the low-pressure system accompanied with the front were still hard to capture, just like any other regional model.

[45] The simulation showed that southwesterly wind brought low-[$CO_2$] air from the midwestern agricultural region to northern Wisconsin on early 15 August 2001. We also found that photosynthesis of the ecosystem in Texas and Oklahoma was shut down in the afternoon of 14 and 15 August 2001 because of extremely high temperatures near the ground surface. A strong [$CO_2$] gradient between the northern Great Plains and southern Great Plains existed in both the model and the observations. $CO_2$-rich air was then transported to Wisconsin and stayed for a short period of time (1800 UT 15 August 2001 to 0000 UT 16 August 2001). The local positive NEEC (6 hours are missing) at the WLEF tower during the daytime of 15 August 2001 and the nighttime of 16 August 2001 because of overcast sky condition together with warm nighttime temperature was responsible for part of the prefrontal [$CO_2$] increase. As the convergence zone of a low-pressure system to the north of the high-[$CO_2$] zone moved slowly to southeast, the enriched air followed accordingly. When cooler air reached Oklahoma and Texas from the north, photosynthesis recovered and soil respiration decreased, thereby signaling the end of the synoptic event of interest.

[46] Both the tower observations and the model simulation showed that at least part of the $CO_2$ temporal variation at the WLEF site, which occurred just prior to the frontal passage, came from horizontal advection. The simulation of atmospheric $CO_2$ variations is dominated by coherent regional anomalies of up to several 10 s of ppm that are produced by regional anomalies in surface weather (especially temperature, humidity, and radiation) and advected by synoptic-scale winds.

[47] The simulated [$CO_2$] was strongly influenced both by local land surface and transport processes over timescale of hours. Thus the reproduction of $CO_2$ signals highly depends on the successful modeling of the ecosystem response, wind fields, and $CO_2$ spatial distribution. A slight difference of $CO_2$ spatial distribution and/or wind fields may misplace the anomalies in time and space. Thus people who utilize tower observed [$CO_2$] in data assimilation must bear in mind that the difference between the observed and simulated [$CO_2$] might be erroneously attributed to either local fluxes or regional transport, when it should be otherwise. If we cannot explain $CO_2$ variations through our understanding of ecophysiology, transport, and/or turbulence, we unfortunately have to filter out the unresolved part and treat it as "noise" before we apply the data in inverse modeling. For example, the $CO_2$ inversions performed by the TransCom 3 [*Gurney et al.*, 2004] strongly deweighted continental observations because, without appropriate filtering, the data contained too much "noise." A goal of future research should be to focus on reproducing the [$CO_2$] variations at continental sites, and properly accounting for ecophysiological and meteorological processes.

[48] **Acknowledgments.** This research was sponsored by a grant from NOAA (NA17RJ1228 Amend. 52). We thank Christopher Still and

Rebecca Powell for the C3/C4 crop fraction map, Shashi B. Verma for the CSP data, and Gabriel G. Katul and Jehn-Yih Juang for the Duke Forest data. We obtained KWKT tower data from Arlyn E. Andrews of NOAA/ESRL GMD and [$CO_2$] data from the Southern Great Plains site from Marc Fischer. Special thanks goes to Saulo Freitas and his colleagues for their SiB-RAMS coupling work. Flux measurements and analyses at the WLEF tower were supported by the Office of Science (BER) U.S. Department of Energy via the Midwestern Regional Center of the National Institutes for Global Environmental Change under cooperative agreement DE-FG03-90ER61010 and via the Terrestrial Carbon Processes program, grant DE-FG02-03ER63681. Mixing ratio measurements were supported by the Atmospheric Chemistry Project of the Climate and Global Change Program of NOAA. Our thanks are given to the two anonymous reviewers and John C. Lin for their inspirational suggestions.

## References


Andres, R. J., G. Marland, I. Fung, and E. Matthews (1996), A 1° × 1° distribution of carbon dioxide emissions from fossil fuel consumption and cement manufacture, 1950–1990, *Global Biogeochem. Cycles*, *10*(3), 419–430.

Arakawa, A., and R. V. Lamb (1977), Computational design of the basic dynamical processes of the UCLA general circulation model, *Methods Comput. Phys.*, *17*, 174–265.

Bender, M., et al. (2002), A large-scale $CO_2$ observing plan: In situ oceans and atmosphere (LSCOP), NOAA OAR special report, 201 pp., Natl. Oceanol. Atmos. Admin., Off. Global Proj., Washington, D. C. (Available at http://www.ogp.noaa.gov/mpe/gcc/co2/)

Benoit, R., M. Desgagne, P. Pellerin, S. Pellerin, Y. Chartier, and S. Desiardins (1997), The Canadian MC2: A semi-Lagrangian, semi-implicit, wideband atmospheric model suited for fine-scale process studies and simulation, *Mon. Weather Rev.*, *125*(10), 2382–2415.

Berger, B. W., K. J. Davis, P. S. Bakwin, C. Yi, and C. Zhao (2001), Long-term carbon dioxide fluxes from a very tall tower in a northern forest: Flux measurement methodology, *J. Ocean. Atmos. Technol.*, *18*, 529–542.

Chan, D., C. W. Yuen, K. Higuchi, A. Shashkov, J. Liu, J. Chen, and D. Worthy (2004), On the $CO_2$ exchange between the atmosphere and the biosphere: The role of synoptic and mesoscale processes, *Tellus, Ser. B*, *56*, 194–212.

Clark, T. L. (1977), A small-scale dynamic model using a terrain-following coordinate transformation, *J. Comput. Phys.*, *24*, 186–215.

Collatz, G. J., J. T. Ball, C. Grivet, and J. A. Berry (1991), Physiological and environmental regulation of stomatal conductance, photosynthesis, and transpiration—A model that includes a laminar boundary layer, *Agric. For. Meteorol.*, *54*, 107–136.

Collatz, G. J., M. Ribascarbo, and J. A. Berry (1992), Coupled photosynthesis-stomatal conductance model for leaves of C4 plants, *Aust. J. Plant Physiol.*, *19*, 519–538.

Cotton, W. R., et al. (2002), RAMS 2001: Current status and future directions, *Meteorol. Atmos. Phys.*, *82*, 5–29.

Davis, K. J., P. S. Bakwin, C. Yi, B. W. Berger, C. Zhao, R. M. Teclaw, and J. G. Isebrands (2003), The annual cycles of $CO_2$ and $H_2O$ exchange over a northern mixed forest as observed from a very tall tower, *Global Change Biol.*, *9*, 1278–1293.

Denning, A. S., G. J. Collatz, C. G. Zhang, D. A. Randall, J. A. Berry, P. J. Sellers, G. D. Colello, and D. A. Dazlich (1996), Simulations of terrestrial carbon metabolism and atmospheric $CO_2$ in a general circulation model: 1. Surface carbon fluxes, *Tellus, Ser. B*, *48*(4), 521–542.

Denning, A. S., M. E. Nicholls, L. Prihodko, I. Baker, P. L. Vidale, K. Davis, and P. Bakwin (2003), Simulated variations in atmospheric $CO_2$ over a Wisconsin forest using a coupled ecosystem-atmosphere model, *Global Change Biol.*, *9*, 1241–1250.

Freitas, S. R., K. M. Longo, M. A. F. Silva Dias, P. L. Silva Dias, R. Chatfield, E. Prins, P. Artaxo, G. A. Grell, and F. S. Recuero (2005), Monitoring the transport of biomass burning emissions in South America, *Environ. Fluid Mech.*, *5*(1–2), 135–167.

Geels, C., S. C. Doney, R. Dargaville, J. Brandt, and J. H. Christensen (2004), Investigating the sources of synoptic variability in atmospheric $CO_2$ measurements over the northern hemisphere continents: A regional model study, *Tellus, Ser. B*, *56*, 35–50.

Global Soil Data Task (2000), *Global Soil Data Products CD-ROM (IGBP-DIS)* [CD-ROM], Int. Geosphere-Biosphere Programme, Data and Inf. Syst., Potsdam, Germany. (Available from Oak Ridge Natl. Lab. Distrib. Active Arch. Cent., Oak Ridge, Tenn., http://www.daac.ornl.gov)

Gloor, M., P. Bakwin, D. Hurst, L. Lock, R. Draxler, and P. Tans (2001), What is the concentration footprint of a tall tower?, *J. Geophys. Res.*, *106*(D16), 17,831–17,840.

Grell, G. A., J. Dudhia, and D. R. Stauffer (1995), A description of the fifth generation Penn State/NCAR mesoscale model (MM5), *NCAR/Tech. Note-398+STR*, pp. 64–72, Natl. Cent. for Atmos. Res., Boulder, Colo.

Gurney, K. R., et al. (2004), Transcom 3 inversion intercomparison: Model mean results for the estimation of seasonal carbon sources and sinks, *Global Biogeochem. Cycles*, *18*, GB1010, doi:10.1029/2003GB002111.

Hansen, M. C., R. S. Defries, J. R. G. Townshend, and R. Sohlberg (2000), Global land cover classification at 1-km spatial resolution using a classification tree approach, *Int. J. Remote Sens.*, *21*(6/7), 1331–1364.

Harrington, J. Y., T. Reisin, W. R. Cotton, and S. M. Kreidenweis (1999), Cloud resolving simulations of Arctic stratus, Part II: Trasition-season clouds, *Atmos. Res.*, *51*, 45–97.

Harrington, J. Y., G. Feingold, and W. R. Cotton (2000), Radiative impacts on the growth of a population of drops within simulated summertime arctic stratus, *J. Atmos. Sci.*, *57*, 766–785.

Holtslag, A. A. M., and B. A. Boville (1993), Local versus nonlocal boundary-layer diffusion in a global climate model, *J. Clim.*, *6*, 1825–1842.

Hurwitz, M. D., M. R. Daniel, P. S. Bakwin, K. J. Davis, W. Wang, C. Yi, and M. P. Butler (2004), Transport of carbon dioxide in the presence of storm systems over a northern Wisconsin forest, *J. Atmos. Sci.*, *61*, 607–618.

Katul, G., R. Leuning, and R. Oren (2003), Relationship between plant hydraulic and biochemical properties derived from a steady-state coupled water and carbon transport model, *Plant Cell Environ.*, *26*(3), 339–350.

Law, R. M., P. J. Rayner, L. P. Steele, and I. G. Enting (2002), Using high temporal frequency data for $CO_2$ inversions, *Global Biogeochem. Cycles*, *16*(4), 1053, doi:10.1029/2001GB001593.

Leff, B., N. Ramankutty, and J. A. Foley (2004), Geographic distribution of major crops across the world, *Global Biogeochem. Cycles*, *18*, GB1009, doi:10.1029/2003GB002108.

Lenschow, D. H., J. Mann, and L. Kristensen (1994), How long is long enough when measuring fluxes and other turbulent statistics?, *J. Ocean. Atmos. Technol.*, *11*, 661–673.

Liu, J., J. M. Chen, J. Cihlar, and W. Chen (2002), Net primary productivity mapped for Canada at 1-km resolution, *Global Ecol. Biogeography*, *11*(2), 115–129.

Louis, J.-F. (1979), A parametric model of vertical eddy fluxes in the atmosphere, *Boundary Layer Meteorol.*, *17*, 187–202.

Lu, L., A. S. Denning, M. A. da Silva Dias, P. Silva Dias, M. Longo, S. R. Freitas, and S. Saatchi (2005), Mesoscale circulation and atmospheric $CO_2$ variation in the Tapajos Region, Para, Brazil, *J. Geophys. Res.*, *110*, D21102, doi:10.1029/2004JD005757.

Marland, G., T. A. Boden, and R. J. Andres (2005), Global, regional, and national $CO_2$ emissions, in *Trends: A Compendium of Data on Global Change*, Carbon Dioxide Inf. Anal. Cent., Oak Ridge Natl. Lab., U.S. Dept. Energy, Oak Ridge, Tenn. (Available at http://cdiac.ornl.gov/trends/emis/em_cont.htm)

Mellor, G. L., and T. Yamada (1974), A hierarchy of turbulence closure models for planetary boundary layers, *J. Atmos. Sci.*, *31*, 1791–1806.

Mellor, G. L., and T. Yamada (1982), Development of a turbulence closure model for geophysical fluid problems, *Rev. Geophys.*, *20*, 851–875.

Mesinger, F., et al. (2006), North American regional reanalysis, *Bull. Am. Meteorol. Soc.*, *87*(3), 343–360.

Nicholls, M. E., A. S. Denning, L. Prihodko, P. L. Vidale, I. T. Baker, K. J. Davis, and P. Bakwin (2004), A multiple-scale simulation of variations in atmospheric carbon dioxide using a coupled biosphere-atmospheric model, *J. Geophys. Res.*, *109*, D18117, doi:10.1029/2003JD004482.

Pielke, R. A., et al. (1992), A comprehensive meteorological modeling system–RAMS, *Meteorol. Atmos. Phys.*, *49*, 69–91.

Sellers, P. J., D. A. Randall, G. J. Collatz, J. A. Berry, C. B. Field, D. A. Dazlich, C. Zhang, G. D. Collelo, and L. Bounoua (1996a), A revised land surface parameterization (SiB2) for atmospheric GCMs, Part I: Model formulation, *J. Clim.*, *9*, 676–705.

Sellers, P. J., S. O. Los, C. J. Tucker, C. O. Justice, D. A. Dazlich, G. J. Collatz, and D. A. Randall (1996b), A revised land surface parameterization (SiB2) for atmospheric GCMs, Part II: The generation of global fields of terrestrial biophysical parameters from satellite data, *J. Clim.*, *9*, 706–737.

Sheridan, P. J., D. J. Delene, and J. A. Ogren (2001), Four years of continuous surface aerosol measurements from the Department of Energy's Atmospheric Radiation Measurement Program Southern Great Plains Cloud and Radiation Testbed site, *J. Geophys. Res.*, *106*(D18), 20,735–20,747.

Takahashi, T., et al. (2002), Global sea-air $CO_2$ flux based on climatological surface ocean $pCO_2$, and seasonal biological and temperature effects, *Deep Sea Res., Part II*, *49*, 1601–1622.

Tripoli, G. J., and W. R. Cotton (1980), A numerical investigation of several factors contributing to the observed variable intensity of deep convection over south Florida, *J. Appl. Meteorol.*, *19*, 1037–1063.

Tripoli, G. J., and W. R. Cotton (1982), The Colorado State University three-dimensional cloud/mesoscale model–1982, Part I: General theoretical framework and sensitivity experiments, *J. Rech. Atmos.*, *16*, 185–220.

Verma, S. B., et al. (2005), Annual carbon dioxide exchange in irrigated and rainfed maize-based agroecosystems, *Agric. For. Meteorol.*, *131*(1–2), 77–96.

Walko, R. L., W. R. Cotton, M. P. Meyers, and J. Y. Harrington (1995), New RAMS cloud microphysics parameterization. Part I: The single-moment scheme, *Atmos. Res.*, *38*, 29–62.

Walko, R. L., et al. (2000), Coupled atmosphere-biophysics-hydrology models for environmental modeling, *J. Appl. Meteorol.*, *39*(6), 931–944.

Wang, J.-W. (2005), Observations and simulations of synoptic, regional, and local variations of atmospheric $CO_2$, M. S. thesis, 98 pp., Colo. State Univ., Boulder.

Wofsy, S. C., and R. C. Harriss (2002), A report of the NACP Committee of the U. S. Carbon Cycle Science Steering Group, N. Am. Carbon Program, Washington, D. C. (Available at http://www.carboncyclescience.gov/)

Yi, C., K. J. Davis, P. S. Bakwin, B. W. Berger, and L. C. Marr (2000), Influence of advection on measurements of the net ecosystem-atmosphere exchange of $CO_2$ from a very tall tower, *J. Geophys. Res.*, *105*(D8), 9991–9999.

I. T. Baker, K. D. Corbin, A. S. Denning, and L. Lu, Department of Atmospheric Science, Colorado State University, Fort Collins, CO 80523, USA.

K. J. Davis, Department of Meteorology, Pennsylvania State University, University Park, PA 16802, USA.

J.-W. Wang, Cooperative Institute for Research in the Environmental Sciences, University of Colorado, Boulder, CO 80309, USA. (jih-wang.wang@colorado.edu)